Petroleum Science 19 (2022) 211–219

Contents lists available at ScienceDirect

Petroleum Science

journal homepage: www.keaipublishing.com/en/journals/petroleum-science

Original Paper

Influence of formation in-situ stress on mechanical heterogeneity of shale through grid nanoindentation

Mao Sheng [a, b, *], Shi-Zhong Cheng [a], Zhao-Hui Lu [b], Ye Zhang [b], Shou-Ceng Tian [a], Gen-Sheng Li [a]

[a] College of Petroleum Engineering, China University of Petroleum-Beijing, 102249, PR China
[b] National and Local Joint Engineering Research Center of Shale Gas Exploration and Development, Chongqing, 401120, PR China

ARTICLE INFO

Article history:
Received 18 November 2020
Accepted 26 September 2021
Available online 22 October 2021

Edited by Yan-Hua Sun

Keywords:
Shale
Heterogeneity
Elastoplasticity
Nanoindentation

ABSTRACT

Mechanical heterogeneity is a major characteristic of the organic-rich shale. The relation between mechanical heterogeneity and formation in-situ stress has been seldomly addressed but important to understand hydraulic fracture propagation, wellbore stability, and hydrocarbon flow. In this paper, the grid nanoindentation technique was used to characterize the heterogeneity of the mechanical properties of Longmaxi organic-rich shales from various burial depths and in-situ stress. The measured elastic modulus and hardness of each sample are deconvolved into three phases including soft phase, medium stiff phase and stiff phase according to mineral category. As the burial depth and corresponding in-situ stress increase, the overall elastic modulus and hardness of the sample enhance. Simultaneously, the percentage of soft minerals decreases, and the probability distribution tends to concentrate through 95% confidence interval evaluation which demonstrates weakened heterogeneity. Furthermore, SEM images provide evidence that extended cracking, initiated cracking, crushing and ductile deforming always occur around indentation imprints. This confirms that even under deep buried depth and high in-situ stress, brittle fracture and ductile deformation can exist synchronously. This paper demonstrates the influence of in-situ stress on the heterogeneity of shale micromechanics.

1. Introduction

Understanding mechanical heterogeneity of organic-rich shales is important for unconventional shale oil and gas reservoirs. The strong heterogeneity on mechanical properties is a major characteristic of organic-rich shale to influence hydraulic fracture propagation, wellbore stability, and hydrocarbon flow (Warpinski and Teufel, 1987; Abouelresh and Slatt, 2012; Hou et al., 2014; Morgan and Einstein, 2017; Zhang et al., 2018). However, the macro-mechanical testing with low space resolution is unable to identify the heterogeneity in microscale because of the complicated mineral composition and highly random distribution.

Nanoindentation, conducted at micrometers scale, have been successfully identified the heterogeneity of rock mechanical properties. An indenter with known hardness and geometry penetrates the testing material with a certain depth. The Young's modulus and hardness of material can be calculated within an indentation cycle according to the force vs. displacement curve (Constantinides et al., 2006; Fischer-Cripps, 2011). To conduct this measurement on heterogeneous materials, grid-indentation and deconvolution approach was proposed to make a statistic analysis (Ulm and Abousleiman, 2006; Abousleiman et al., 2007). Li et al., (2018) used nanoindentation to characterize the mechanical properties of organic matter. The type and thermal maturity of kerogen influence its Young's modulus and hardness. An advanced nanoindentation mapping technique was developed with the capacity to map the distribution of Young's modulus and hardness (Yang et al., 2017). Integrated with Scanning Electron Microscopy/Energy Dispersive X-Ray Spectroscopy (SEM-EDS), nanoindentation becomes more flexible to quantify the mechanical properties of individual minerals and mineral clusters (Deirieh et al., 2012; Bennett et al., 2015; Akono and Kabir, 2016). Although nanoindentation has become a practical tool to understand the heterogeneity of mechanical properties of shale, yet the effects of formation in-situ stress on the mechanical heterogeneity and elastoplastic

* Corresponding author.
E-mail address: shengmao@cup.edu.cn (M. Sheng).

https://doi.org/10.1016/j.petsci.2021.10.006

behaviors have rarely been addressed.

In this paper, the grid nanoindentation approach was used to quantify the heterogenous distribution of Young's modulus and hardness at different burial depths and formation in-situ stress. Further, the deconvolution method was applied to distinguish three mineral phases with distinct hardness and Young's modulus. The indentation topography was imaged by SEM with high resolution of 10 μm. The influence of formation in-situ stress on mechanical properties was particularly discussed. Results confirmed that in-situ stress controls the heterogeneity of organic-rich shale and the high in-situ stress reduces the heterogeneity of shale mechanical properties.

2. Materials and methods

2.1. Material and specimen preparation

Three distinct shale samples were collected from the downhole cores at Lower Silurian Longmaxi Formation, Sichuan Basin, China. The vertical burial depth of N-213, Z-202 and N-222 are 2502.0, 3858.3 and 4278.7 m, respectively.

Their mineral composition interpreted from XRD tests was compared in Table 1. XRD tests were conducted according to the Standard SY/T 5163-2010. Results indicate that the target samples are the classical black shale containing much quartz and clay minerals. Samples N-213 and N-222 are mainly composed of clay minerals while Sample Z-202 is mainly composed of quartz minerals.

The cubical specimen (5 mm length × 5 mm width × 1 mm height) were extracted from the shale samples. The sanding papers meshing 180#, 400#, 1000#, 2000#, and 4000# were utilized to polish samples reaching surface roughness of 0.5 μm. Then, a high energy argon ion beam (Leica EM RES 102) was used at the polishing angle of 4.5°, current of 2 mA to polish the specimen surface. Polishing voltage was set at 5 kV and 2 kV alternately to keep surface roughness the minimum. The standard polishing approach was applied to expose the original microstructure of the rock, ensure required roughness for nanoindentation test and facilitate accurate observation under SEM. The reference lines were marked on the sample surface in order to locate the same test area in nanoindentation and SEM. The key is to ensure that the upper and lower sample surfaces are parallel, and the upper surface has the required smoothness. The surface roughness of shale samples evaluated by atomic force microscopy (AFM) is controlled in the range of 3.2–15.6 nm

2.2. Experimental design

Grid nanoindentation tests were conducted in a randomly selected area on the polished surface of the cubical sample to measure Young's modulus and hardness of grid points. Grid nanoindentation guarantees randomness and data sufficiency. The abundant data ensure quantitative and qualitative measurement and analysis on composite. Furthermore, statistical analysis could express overall mechanical properties from a large number of individual data. Deconvolution approach was used to obtain the probability distributions of mechanical properties of different phases. Finally, SEM was conducted to visualize the indentation imprints and understand the elastoplastic deformation behaviors.

The grid nanoindentation was run through the commercial equipment of Keysight Nano Indenter G200. Particularly, the continuous stiffness measurement (CSM) mode was selected to continuously measure the mechanical properties over the indentation depth. CSM is a mature technique mode in nanoindentation, which applies harmonic oscillator to indenter. A sinusoidal load was conducted with a constant frequency. The highest load in each load cycle is higher than that in the previous cycle, as shown in Fig. 1(b). So that the load and penetrating depth increase. In each load cycle, the elastic modulus and hardness at that depth are obtained by the same calculation method as follows (Phani et al., 2020). Due to the complex composition and strong heterogeneity of shale, the mechanical properties of distinct minerals vary greatly. A Berkovich diamond indenter was selected because of its high spring constant range and suitability for complex materials with a wide range of elastic modulus. The indenter was used with a maximum loading of 30 mN and a maximum effective penetrating depth of 25 μm. Indenter load was conducted at a constant strain rate of 0.05 s^{-1} and a frequency of 45 Hz. Ultimate indent depth was set at 3000 nm to enable multi-scale measurement of minerals and mineral phases. Room temperature was controlled as 25 °C (±0.5 °C).

Fig. 1 illustrates a schematic of grid nanoindentation test. The indenter tip penetrates the sample surface until the indentation depth reaches a prescribed magnitude. With increasing indentation depth, the material deformation transforms from elastic to plastic deformation. During indenter withdrawal, only elastic deformation recovers. The area enclosed by the loading, holding and unloading curves in the load-displacement curve represents the irreversible energy. It is worth noting that the energy not only consists of the plastic deformation energy of indentation point but also the fracture energy of the generated or extended cracks (Cheng et al., 2002). A grid nanoindentation scheme was proposed to obtain a statistically significant evaluation of mechanical properties. As shown in Fig. 1(c), a 10 × 10 indentation grid was assigned on the specimen surface. The individual points were separated by 90 μm, which was adequate to eliminate interaction among individual points and also reach the scale to obtain the average response of the composite (Ulm and Abousleiman, 2006).

From the load-displacement curve, Young's modulus and hardness were calculated through the following equations (Oliver and Pharr, 1992; Li et al., 2019):

$$\frac{1}{E_r}=\frac{(1-\nu)^2}{E}+\frac{(1-\nu_i)^2}{E_i} \tag{1}$$

$$E_r=\frac{\sqrt{\pi}}{2}\frac{S}{\sqrt{A_c}} \tag{2}$$

Table 1
Mineral composition of three distinct core samples.

Sample	Depth, m	Composition, wt%						
		Quartz	Clay	Calcite	Dolomite	Feldspar	Pyrite	Others
N-213	2502.0	31.2	39.3	8.5	7.5	10.4	3.1	/
Z-202	3858.3	48.1	31.7	2.3	0.2	9.3	1.2	7.2
N-222	4278.7	34.6	39.5	10.6	/	13.2	2.1	/

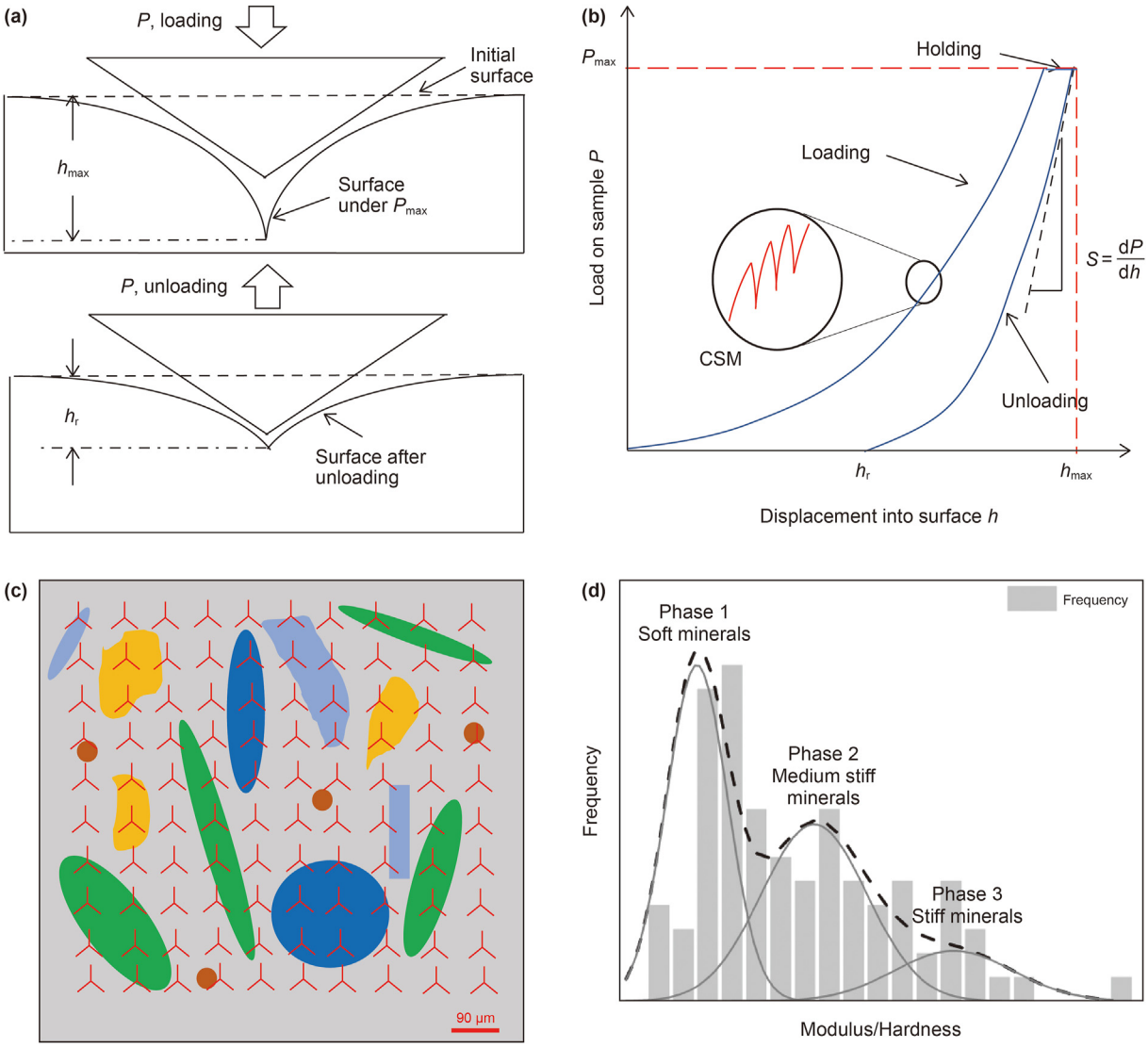

Fig. 1. Nanoindentation schematic: **(a)** Penetration diagram; (**b**) Nanoindentation load on sample-displacement into surface curve and continuous stiffness measurement (CSM) diagram; (**c**) Grid indentation points; (**d**) Diagram of deconvolution method to identify various phases.

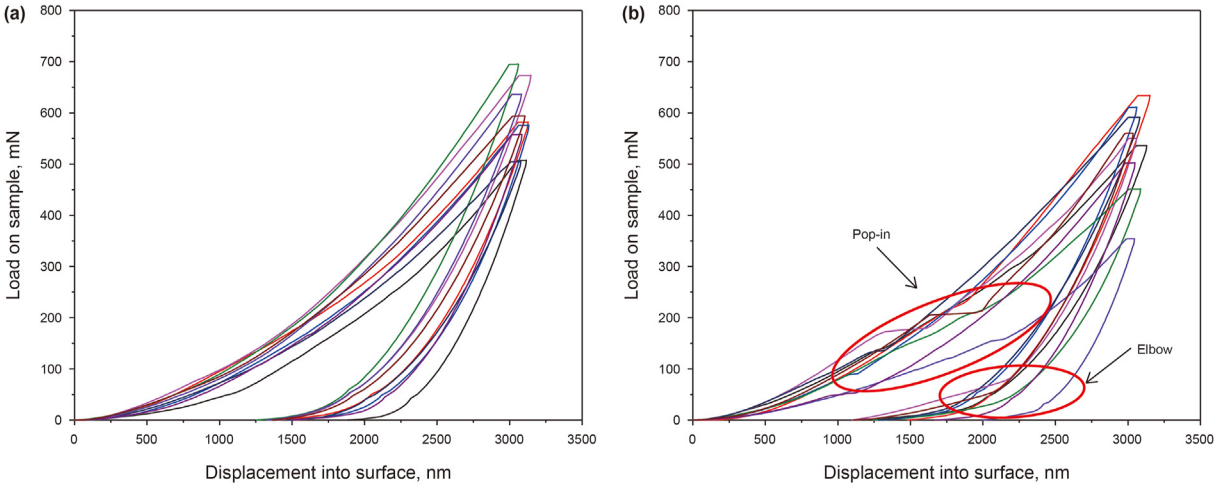

Fig. 2. Typical load-displacement curve from nanoindentation tests.

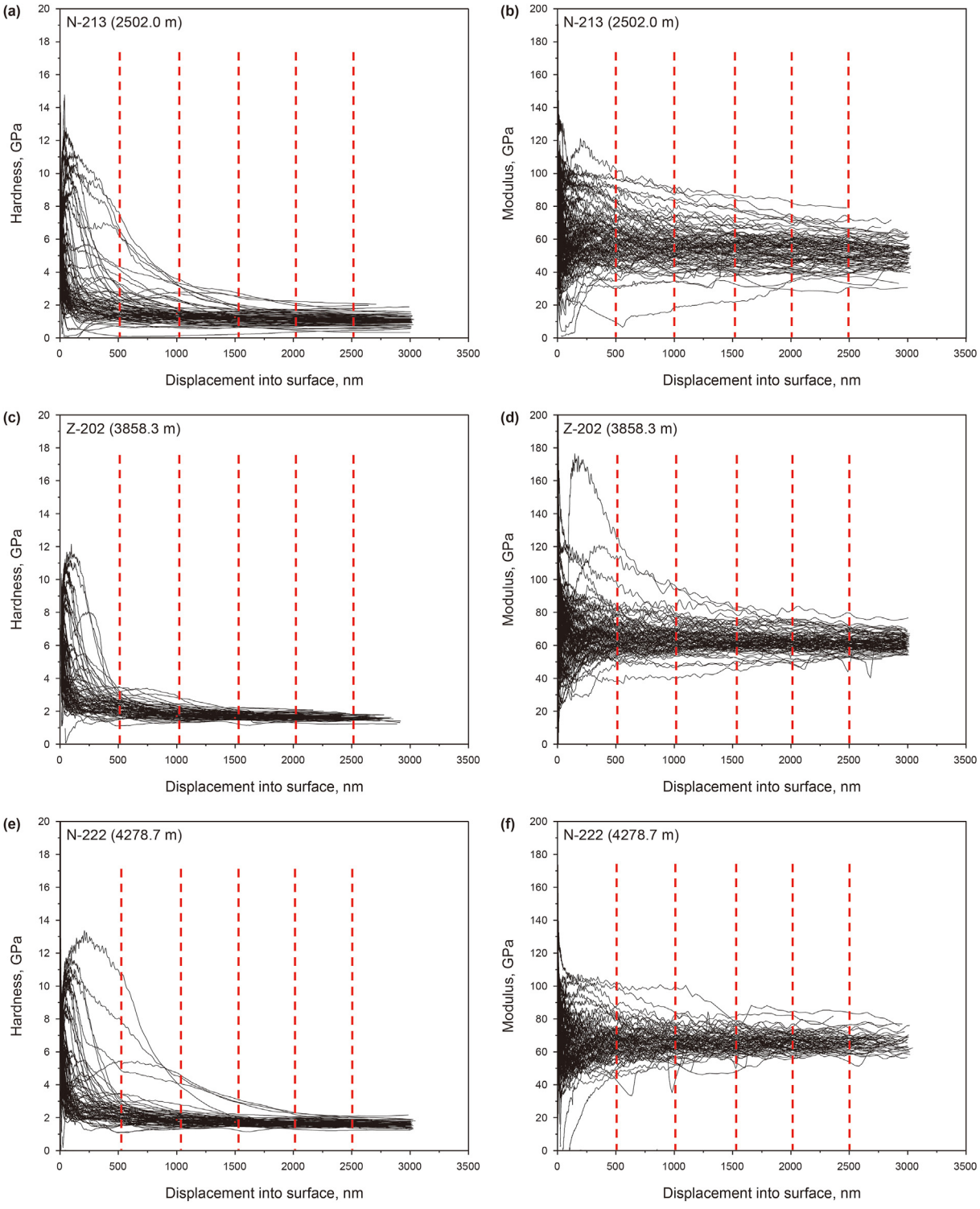

Fig. 3. CSM modulus and hardness results of each indentation point in samples N-213, Z-202 and N-222.

$$H = \frac{P_{\max}}{A_c} \tag{3}$$

$$S = \frac{dP}{dh}|_{h=h_{\max}} \tag{4}$$

where E_r is the reduced modulus; ν is Poisson's ratio of the sample; E is Young's modulus of the sample; ν_i is Poisson's ratio of the probe; E_i is Young's modulus of the probe; $P_{\max}$ is the maximum load on sample. In each CSM circle, $P_{\max}$ is also the maximum load in each circle. S is the stiffness, which could be calculated from unloading curve. A_c is the projected contact area related to contact depth and tip shape. For Berkovich indenters, $A_c = 24.56{h_c}^2 + Ch_c$. C is a constant obtained in the calibration.

The deconvolution approach was used to identify mineral phases with distinct hardness and Young's modulus (Kumar et al.,

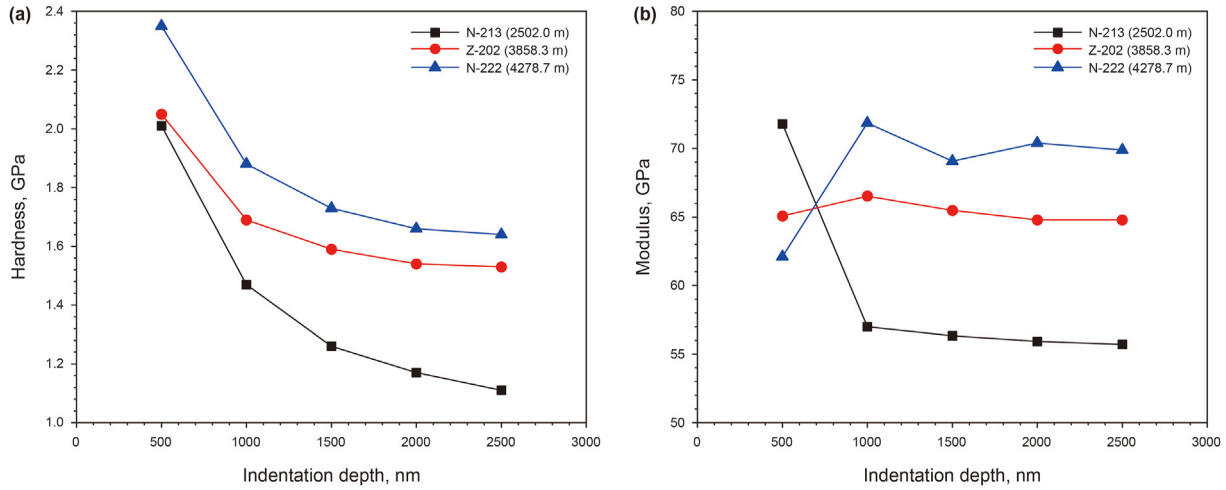

Fig. 4. The average value of the overall data of modulus and hardness measured by CSM at different indentation depths.

2012; Veytskin et al., 2017). Those data were divided into three phases, which is adequate to show characteristics of different mineral phases. In detail, it includes stiff, medium stiff, and soft phases. Generally, the stiff phase mainly include silicates and sulfides, the medium stiff phase covers carbonates and the soft phase can be clay minerals and Kerogen materials. By assuming each phase is available to be characterized by a Gaussian distribution, the distribution of mechanical properties is shown in Fig. 1(d). Each phase has a corresponding probability density function and similar mechanical properties.

The Gaussian distribution can be written as (Ulm and Abousleiman, 2006):

$$p_i(x|\theta_i) = \frac{1}{\sqrt{2\pi}\sigma_i}\exp[-\frac{(x-u_i)^2}{2{\sigma_i}^2}] \tag{5}$$

where $\theta_i = (u_i, {\sigma_i}^2)$; u_i is the arithmetic mean of all values for phase i and ${\sigma_i}^2$ is the variance. Consequently, the theoretical probability density function (PDF) can be given as:

$$P(x|\theta) = \sum_{i=1}^{j} f_i p_i(x|\theta_i) \tag{6}$$

where f_i is the surface friction occupied by phase i, and satisfied with $\sum_{i=1}^{j} f_i = 1$.

For the deconvolution analysis, the expectation-maximization (EM) algorithm was used to optimize the best-fitted mixture Gaussian distributions (Dempster et al., 1977; Moon, 1996). A programming code combined EM algorithm and Gaussian mixture model was developed in this study. The EM algorithm contains two main steps. E-step is the first main step to calculate the posterior probability that point x_i belongs to phase j.

$$\omega_{ij} = \frac{\alpha_j P(x_i|\theta_j)}{\sum_{j=1}^{J} \alpha_j P(x_i|\theta_j)}, \quad i = 1,2,3...N; \ j = 1,2,3...J \tag{7}$$

Here the phase number is three, so $J = 3$. M-step is the second one, which is to conduct maximum likelihood estimation by updating values for parameters given by current distribution.

$$\alpha_j = \frac{1}{n}\sum_{i=1}^{n} \omega_{ij} \tag{8}$$

$$\mu_j = \frac{\sum_{i=1}^{N} \omega_{ij} x_i}{\sum_{i=1}^{N} \omega_{ij}} \tag{9}$$

$$\sigma^2 = \frac{\sum_{i=1}^{N} \omega_{ij}(x_i - \mu_j)^2}{\sum_{i=1}^{N} \omega_{ij}} \tag{10}$$

3. Results

3.1. Nanoindentation

Fig. 2 shows the typical load-displacement curves observed from nanoindentation testing. The “pop-in” phenomena demonstrate the creation of micro-cracking or encounters with pores or micro-fractures. The “elbow” events in unloading curve are caused by material expansion due to phase transformation (Domnich et al., 2000). By examining all the load-displacement curves, ratios of final indentation depth to maximum indentation depth are less than 0.7, thus the pile-up phenomenon does not exist. This indicates that the original data are not required to be corrected (Oliver and Pharr, 1992).

Fig. 3 illustrates the correlations of the hardness and Young’s modulus against indentation depth, respectively. Results show that the magnitudes of both hardness and Young’s modulus are highly dependent on the indentation depth. For the indentation depth between 0 and 2000 nm, the modulus demonstrated relatively significant but gradually less obvious fluctuation for each indentation point. This indicates that as the indentation depth increases, the indenter encounters more different minerals. The mixture of various minerals decreases the fluctuation of Young's modulus and hardness for the sample. Solely depending on one kind of mineral demonstrates significant variations and fluctuations at the very

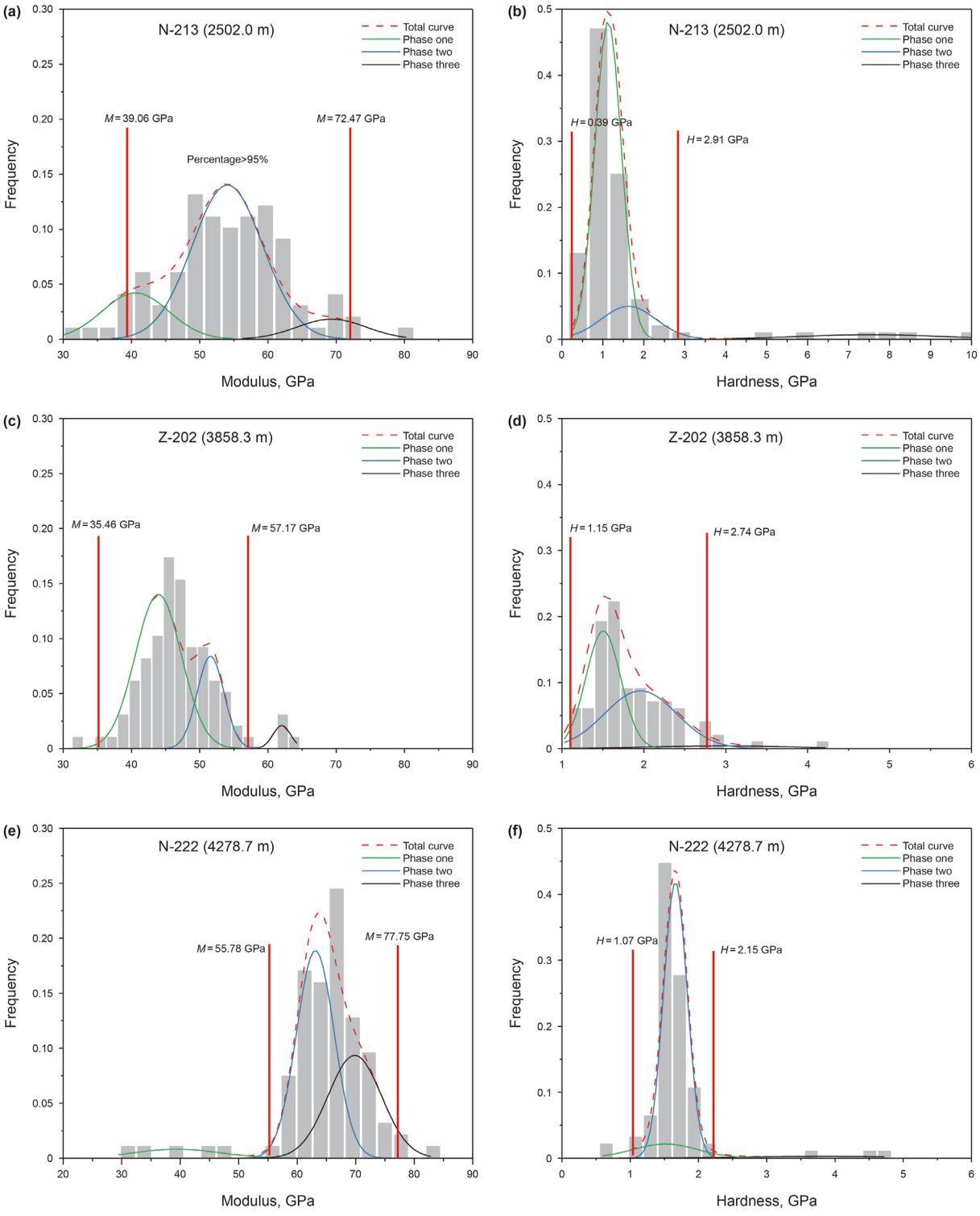

Fig. 5. Deconvolution results of modulus and hardness for each phase under different confining stress conditions. The interval enclosed by the red straight line represents the data interval accounting for more than 95%.

beginning of the indentation process. The encounter with much different minerals can be associated with the gradually increased indented area, which means that the larger indented area might result in the contact with more minerals. As the indentation depth increases from 2000 nm to 3000 nm, the modulus curve eventually converges to a small range, which elucidates that the indentation area has reached the scale of the mineral phase (Luo et al., 2020). Moreover, it should be noticed that the ultimate convergence range of each curve is different due to the heterogeneity of mineral phases in shale.

The indentation depth was set at 3000 nm for each point, 500 nm was set as the step to calculate the average of mechanical

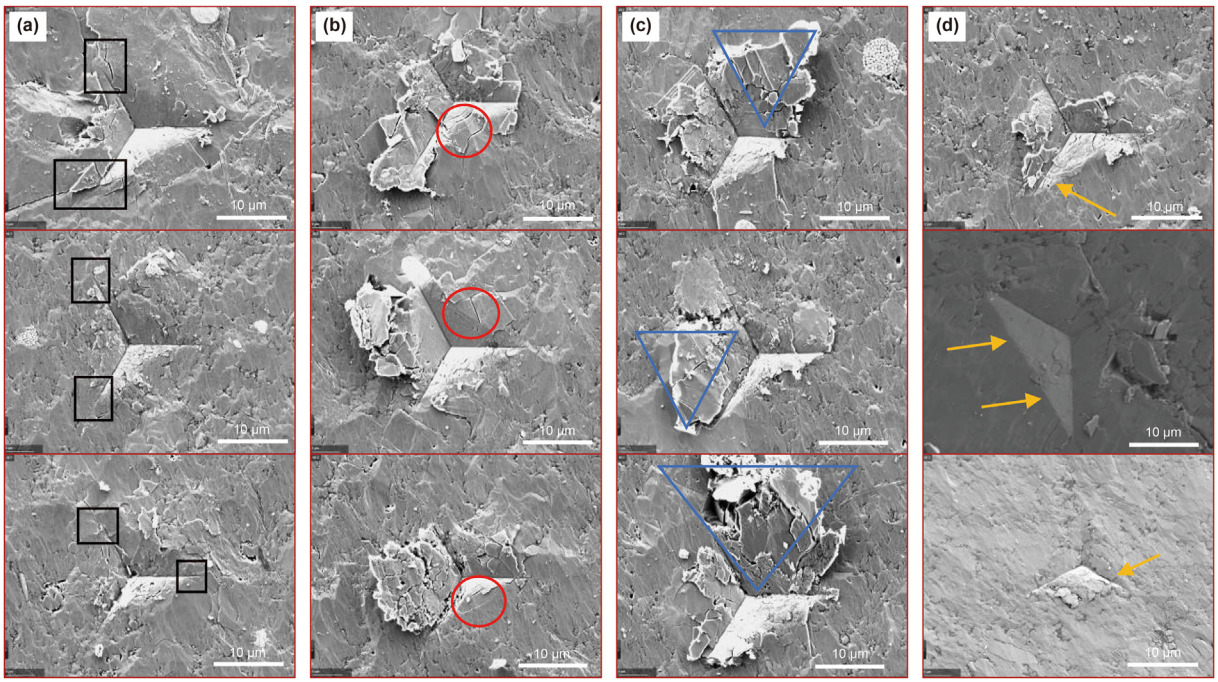

Fig. 6. SEM images of the specific indentations in all samples. (**a**) The black rectangular area is the extension cracks at the tip of the indentation. (**b**) The red ellipse area is the indentation-generated irregular cracks. (**c**) The blue triangle area is the failure areas. (**d**) The yellow arrow points to the ductile deformation.

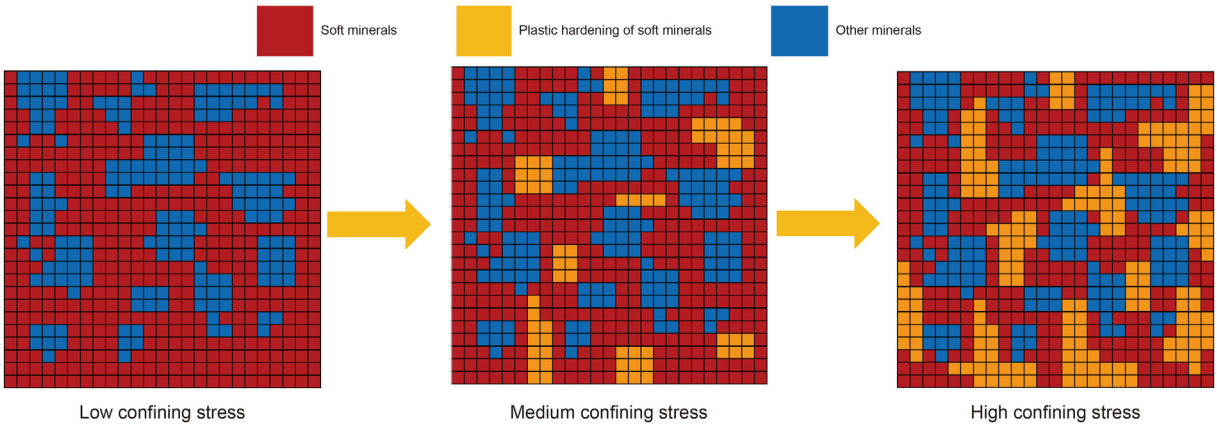

Fig. 7. Schematic diagram of the mechanism of in-situ stress on the mechanical heterogeneity of shale. The red area represents soft phase like organic matter and clay while the blue area represents stiff phase. The yellow area shows the transition of mechanical properties from soft to stiff because of the material hardening.

properties in every sample. The average of the overall modulus and hardness data measured at 500, 1000, 1500, 2000, 2500 nm depths is shown in Fig. 4. Under different in-situ stresses, as the indentation depth increases, the overall averages of modulus and hardness gradually converge, which is consistent with the results in Fig. 3.

The frequency distribution histograms and deconvolution results of Young's modulus and hardness for samples are constructed in Fig. 5. Total curve is the sum of Gaussian distribution curves of three mineral phases. Young's modulus are in the range of 33.1–80.2 GPa, 30.8–64.2 GPa, and 33.6–84.4 GPa respectively. Hardness is in the range of 0.4–10.35 GPa, 0.95–4.21 GPa, and 0.6–4.89 GPa. A large amount of nanoindentation data were divided into three mineral phases. Each phase, as illustrated in Fig. 1(d), has one dominant property value. These values vary with increasing confining stress. The probability density distribution histogram can intuitively show the distribution of mechanical properties in different intervals. Also, it is the basic reference data for sub-phase curves. As the burial depths of the three shale samples increase in the order of N-213, Z-202 and N-222, high in-situ stress weakens the heterogeneity of the mechanical properties of the downhole shale. As shown in Fig. 5, the interval enclosed by the red straight line represents the data interval accounting for more than 95%. In sample N-222, under high in-situ stress, this interval is narrower, indicating that the mechanical properties are more concentrated. The mean value and standard deviation of Gaussian distributions of Young's modulus and hardness for each phase after processing through the Python program are shown in Table A1 (Appendix A).

3.2. SEM evidence of elastoplastic behavior at indentation points

Mineral phases respond differently to indenter stress under in-situ stress conditions. In order to obtain the elastoplastic response of mineral phases, a high-resolution scanning electron microscope

was used to image the indentation point morphology, as shown in Fig. 6. The black rectangular area is the extension cracks at the tip of the indentation. The red ellipse area is the indentation-generated irregular cracks. The blue triangle area is the failure areas. The yellow arrow points to the ductile deformation. The deformation and failure morphology of the indentation points have strong non-uniformity. It is related to the mineral compositions around the indentation point. The reason is that in the SEM images with a scale of 10 μm, the deformation appears along the edge line of the indentation, but no cracks are generated.

4. Discussion

A strong heterogeneity of mechanical properties in organic-rich shale has been evaluated and confirmed in this study. Moreover, high in-situ stress weakens this heterogeneity of the mechanical properties of the downhole shale. As illustrated in Fig. 5, a non-uniform shift of Young's modulus and the corresponding frequency of the individual phases are observed in samples N-213 and N-222. The compositions of the two samples are similar, but the burial depths are different. The deconvolution result shows that the frequency of the first phase of N-222 is less than that of N-213, which indicates high in-situ stresses lead soft minerals to be hardened. 95% confidence interval evaluation in Fig. 5 elucidates weakening effect of in-situ stress on the heterogeneity of the mechanical properties of organic-rich shale. Fig. 7 shows the mechanism of confining stresses on shale heterogeneity. The red area represents soft minerals, organic matter and clay, and the blue area represents other minerals. The yellow area shows the hardening effect of in-situ stresses on soft minerals, which demonstrates that the high in-situ stress weakens the heterogeneity of the mechanical properties of the downhole shale.

Although the heterogeneity of shale weakened with the increase of in-situ stress, brittle failure and ductile deformation (Fan et al., 2019) still coexist around indentation imprints (Fig. 6). Furthermore, "pop-in" and "elbows" phenomenon commonly happened in nanoindentation (Fig. 2), which exhibits that the indenter encountered heterogeneous mineral compositions during the indenting process. This indicates that the heterogeneity of shale still exists under high in-situ stress environment. Heterogeneity of shale has been confirmed through mesoscale indentation and macroscale indentation tests (Dong and Chen, 2017). The finer the test scale, the higher the heterogeneity of the shale. Macroscopic failure in shale is the accumulation results of mesoscopic and microscope damage, fracture and fragmentation. Mechanical properties and in-situ stress environment would influence hydraulic fracturing framework cause complexity of fracture network in deep shale reservoirs.

5. Conclusions

Multi-scale assessment of mechanical heterogeneity of Longmaxi organic-rich shale was conducted by nanoindentation and SEM. Nanoindentation results demonstrate the magnitudes of both hardness and Young's modulus are highly dependent on the indentation depth. Three mineral phases are categorized through modulus and hardness by nanoindentation. Combined statistical analysis, it is concluded that high in-situ stress will weaken the heterogeneity of organic-rich shale. SEM images provide evidence that extended cracking, initiated cracking, crushing and ductile deforming always occur around indentation imprints. This confirms that even under deep buried depth and high in-situ stress, brittle fracture and ductile deformation can exist synchronously. Particularly, the variable and uneven distribution of minerals with wildly-ranged mechanical properties likely regulates hydraulic fracture complexity even in deep reservoirs with high in-situ stress. In the next step, we will perform numerical simulations based on micromechanical data to explain the mechanism of microcracks initiation and extension under stresses.

Acknowledgments

This work was financially supported by National Natural Science Foundation of China (No. U19B6003; No. 52074315)

Appendix A

Table A1
Mean and standard deviation of each Gaussian distribution

Parameter	Identifier	Sample		
		Z-202	N-213	N-222
Mean modulus, GPa	Phase one	43.93	41.48	40.74
	Phase two	51.37	63.33	54.24
	Phase three	62.74	69.98	69.29
Standard deviation of modulus	Phase one	3.23	8.57	3.32
	Phase two	2.15	2.04	5.27
	Phase three	1.69	3.81	4.81
Mean hardness, GPa	Phase one	1.51	1.51	1.09
	Phase two	1.96	1.64	1.60
	Phase three	2.96	3.85	7.50
Standard deviation of hardness	Phase one	0.47	1.32	0.37
	Phase two	0.84	0.52	0.65
	Phase three	1.23	0.69	2.13

References

Abouelresh, M.O., Slatt, R.M., 2012. Lithofacies and sequence stratigraphy of the Barnett shale in east-central fort worth basin, Texas. AAPG (Am. Assoc. Pet. Geol.) Bull. 96 (1), 1–22. https://10.1306/04261110116.

Abousleiman, Y.N., Tran, M.H., Hoang, S., Bobko, C.P., Ortega, A., Ulm, F.-J., 2007. Geomechanics field and laboratory characterization of the woodford shale: the next gas play. In: SPE Annual Technical Conference and Exhibition, November, Anaheim. California, U.S.A. http://10.2118/110120-ms.

Akono, A.-T., Kabir, P., 2016. Microscopic fracture characterization of gas shale via scratch testing. Mech. Res. Commun. 78, 86–92. https://10.1016/j.mechrescom.2015.12.003.

Bennett, K.C., Berla, L.A., Nix, W.D., Borja, R.I., 2015. Instrumented nanoindentation and 3D mechanistic modeling of a shale at multiple scales. Acta Geotechnica 10 (1), 1–14. https://10.1007/s11440-014-0363-7.

Cheng, Y.-T., Li, Z., Cheng, C.-M., 2002. Scaling relationships for indentation measurements. Philos. Mag. A 82, 1821–1829. https://10.1080/01418610210135043.

Constantinides, G., Ravi Chandran, K.S., Ulm, F.J., Van Vliet, K.J., 2006. Grid indentation analysis of composite microstructure and mechanics: principles and validation. Mater. Sci. Eng., A 430 (1-2), 189–202. https://10.1016/j.msea.2006.05.125.

Deirieh, A., Ortega, J.A., Ulm, F.J., Abousleiman, Y., 2012. Nanochemomechanical assessment of shale: a coupled WDS-indentation analysis. Acta Geotechnica 7 (4), 271–295. https://10.1007/s11440-012-0185-4.

Dempster, A.P., Laird, N.M., Rubin, D.B., 1977. Maximum likelihood from incomplete data via the EM algorithm. J. Roy. Stat. Soc. B 39 (1), 1–22. https://10.1111/j.2517-6161.1977.tb01600.x.

Domnich, V., Gogotsi, Y., Dub, S., 2000. Effect of phase transformations on the shape of the unloading curve in the nanoindentation of silicon. Appl. Phys. Lett. 76 (16), 2214–2216. https://10.1063/1.126300.

Dong, G., Chen, P., 2017. A comparative experimental study of shale indentation fragmentation mechanism at the macroscale and mesoscale. Adv. Mech. Eng. 9 (8), 168781401772624. https://10.1177/1687814017726244.

Fan, M., Jin, Y., Chen, M., Geng, Z., 2019. Mechanical characterization of shale through instrumented indentation test. J. Petrol. Sci. Eng. 174, 607–616. https://doi.org/10.1016/j.petrol.2018.11.083.

Fischer-Cripps, A.C., 2011. Nanoindentation Testing. Springer, New York.

Hou, B., Cheng, W., Chen, M., Tan, P., Yang, L., 2014. Experiments on the non-planar extension of hydraulic fractures in fractured shale gas reservoirs. Nat. Gas. Ind. 34, 81–86. https://10.3787/j.issn.1000-0976.2014.12.011.

Kumar, V., Sondergeld, C.H., Rai, C.S., 2012. Nano to macro mechanical characterization of shale. In: SPE Annual Technical Conference and Exhibition, 2012/1/1/. San Antonio, Texas, USA. https://10.2118/159804-MS.

Li, C., Ostadhassan, M., Abarghani, A., Fogden, A., Kong, L., 2019. Multi-scale evaluation of mechanical properties of the Bakken shale. J. Mater. Sci. 54 (3),

2133–2151.
Li, C., Ostadhassan, M., Gentzis, T., Kong, L., Carvajal-Ortiz, H., Bubach, B., 2018. Nanomechanical characterization of organic matter in the Bakken formation by microscopy-based method. Mar. Petrol. Geol. 96, 128–138. https://10.1016/j.marpetgeo.2018.05.019.
Luo, S., Lu, Y., Wu, Y., Song, J., DeGroot, D.J., Jin, Y., Zhang, G., 2020. Cross-scale characterization of the elasticity of shales: statistical nanoindentation and data analytics. J. Mech. Phys. Solid. 140, 103945. https://doi.org/10.1016/j.jmps.2020.103945.
Moon, T.K., 1996. The expectation-maximization algorithm. IEEE Signal Process. Mag. 13 (6), 47–60. https://10.1109/79.543975.
Morgan, S.P., Einstein, H.H., 2017. Cracking processes affected by bedding planes in Opalinus shale with flaw pairs. Eng. Fract. Mech. 176, 213–234. https://10.1016/j.engfracmech.2017.03.003.
Oliver, W., Pharr, G., 1992. An improved technique for determining hardness and elastic modulus using load and displacement sensing indentation experiments. J. Mater. Res. 7, 1564–1583. https://10.1557/JMR.1992.1564.
Phani, P.S., Oliver, W.C., Pharr, G.M., 2020. Understanding and modeling plasticity error during nanoindentation with continuous stiffness measurement. Mater. Des. 194, 108923. https://doi.org/10.1016/j.matdes.2020.108923.
Ulm, F.-J., Abousleiman, Y., 2006. The nanogranular nature of shale. Acta Geotechnica 1 (2), 77–88. https://10.1007/s11440-006-0009-5.
Veytskin, Y.B., Tammina, V.K., Bobko, C.P., Hartley, P.G., Clennell, M.B., Dewhurst, D.N., Dagastine, R.R., 2017. Micromechanical characterization of shales through nanoindentation and energy dispersive x-ray spectrometry. Geomechanics for Energy and the Environment 9, 21–35. https://10.1016/j.gete.2016.10.004.
Warpinski, N., Teufel, L., 1987. Influence of geologic discontinuities on hydraulic fracture propagation. J. Pet. Technol. 39 (02), 209–220. https://doi.org/10.2118/13224-PA.
Yang, J., Hatcherian, J., Hackley, P.C., Pomerantz, A.E., 2017. Nanoscale geochemical and geomechanical characterization of organic matter in shale. Nat. Commun. 8 (1), 2179. https://10.1038/s41467-017-02254-0.
Zhang, L., Li, B., Jiang, S., Xiao, D., Lu, S., Zhang, Y., Gong, C., Chen, L., 2018. Heterogeneity characterization of the lower Silurian Longmaxi marine shale in the Pengshui area, South China. Int. J. Coal Geol. 195, 250–266. https://doi.org/10.1016/j.coal.2018.05.015.